

Experimental demonstration of direct terahertz detection at room-temperature in AlGaN/GaN asymmetric nanochannels

Paul Sangaré,¹ Guillaume Ducournau,¹ Bertrand Grimbert,¹ Virginie Brandli,¹ Marc Faucher,¹ Christophe Gaquière,¹ Ana Íñiguez-de-la-Torre,² Ignacio Íñiguez-de-la-Torre,² J. F. Millithaler,² Javier Mateos,² and Tomas González²
¹IEMN/Université de Lille 1, UMR CNRS 8520, Avenue Poincaré, 59650 Villeneuve d'Ascq, France
²Departamento de Física Aplicada, Universidad de Salamanca, Plaza de la Merced s/n, 37008 Salamanca, Spain

(Received 2 October 2012; accepted 17 December 2012; published online 15 January 2013)

The potentialities of AlGaN/GaN nanodevices as THz detectors are analyzed. Nanochannels with broken symmetry (so called self switching diodes) have been fabricated for the first time in this material system using both recess-etching and ion implantation technologies. The responsivities of both types of devices have been measured and explained using Monte Carlo simulations and non linear analysis. Sensitivities up to 100 V/W are obtained at 0.3 THz with a 280 pW/Hz^{1/2} noise equivalent power. © 2013 American Institute of Physics. [<http://dx.doi.org/10.1063/1.4775406>]

The field of Terahertz Science and Technology is gaining international interest due to its broad potential applications, ranging from ultra high speed wireless transmission systems to medical diagnostic, industrial quality control, security-screening tools, THz astronomy, high speed communications, or pharmacology.^{1,2} In the field of electronics, the efforts in order to reach the THz frequencies have been devoted to the top-down approach, reducing the size of devices down to the nanometer range in order to increase the operational speed. However, the “THz gap” is not covered yet by transistors, since the reduction of the gate length does not lead to a sufficient increase of the cut-off frequency as predicted by the traditional scaling rules. On the other hand, since the photon energy of terahertz radiation is smaller than the thermal energy at room temperature, photonic devices as quantum cascade lasers are operational only at cryogenic temperatures. The development of room temperature, compact and low-cost semiconductor devices covering the “THz gap” is still one of the challenges of nanoelectronics and will be of great interest for many applications. Since the pioneering work of Grischkowsky³ of photo-conductive devices for pulsed THz systems, great efforts are still conducted to achieve room temperature compact THz emitters and detectors. Several devices have been reported⁴ as multiplication chains, photomixers, non-linear optics, and quantum cascade lasers. Recent developments on resonant tunneling diodes (RTD), which can work both as THz emitter and detector, lead to 1.1 THz room temperature continuous wave (CW) emission with μ W output powers.⁵ In direct THz detection systems such as Golay cells,^{6,7} pyroelectric detectors,⁸ or microbolometer elements (VOx,⁹ Bi,¹⁰ Nb¹¹), which are currently used in THz focal plane arrays, the response time is relatively long and responsivities are not very high. Present state-of-the-art for detection of high frequency radiation is achieved by Schottky diodes,¹² where electrical rectification of the incident electromagnetic radiation is realized through nonlinear current-voltage characteristic. However, Schottky diodes operating at THz frequencies require advanced materials and challenging fabrication (ultra-low electron transit

times and parasitic elements to be able to work at these frequencies). Among emerging electronic detectors coming from nanotechnology, nanowire field-effect transistors¹³ based on the theory first proposed by Dyakonov and Shur,¹⁴ are a possible alternative. Based on a different concept, the self-switching diode¹⁵ (SSD) has been proposed to produce planar asymmetric non-linear devices. The SSD consists of two insulating L-shaped trenches which define an asymmetric nanochannel in a semiconductor material. Adjusting the nanochannel width results in a non-linear, diode like, current voltage (I-V) characteristic. These components (based on GaAs and InGaAs heterojunctions) have been demonstrated as room temperature detectors at millimeter¹⁶ and terahertz frequencies.¹⁷

In this letter, we propose for the first time to exploit AlGaN/GaN nanochannels potentialities to realize room temperature THz nanodetectors working at zero bias. This is the first step towards the development of a complete room-temperature integrated THz emitter/detector system since SSDs are also theoretically expected to produce THz emission by means of Gunn oscillations.¹⁸ Here, we experimentally demonstrate their detection capabilities.

Figure 1(a) shows the typical geometry of the SSDs, where the etching of the trenches is used to define an asymmetric nanochannel in an AlGaN/GaN heterostructure. Figure 1(b) shows the geometry of the simulation domain with the parameters involved in the “top-view” Monte Carlo (MC) simulation: the “virtual” doping N_{Db} and a negative surface charge density σ . L and W are the length and width of the nanochannel, respectively, W_H the width of the horizontal trench, and W_V the width of the vertical trench.

To explain and analyze the nanochannel behavior, a semi-classical MC simulation self-consistently coupled with a Poisson solver is used.¹⁹ The modeling of the SSDs would require a 3D simulation to exactly describe the influence of the lateral surface charges and the actual layer structure. To avoid the complexity of 3D models, instead we performed “top-view” 2D simulations of the channel only, and the influence of the fixed charges present in the layer structure

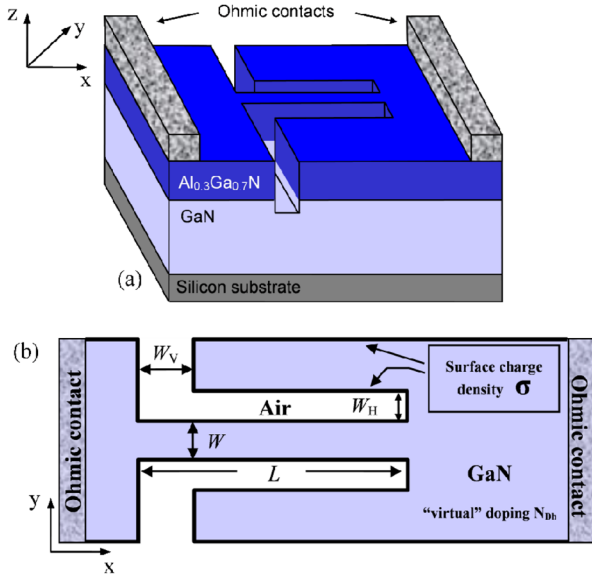


FIG. 1. (a) Three-dimensional geometry of the SSDs. (b) “Top view” geometry as considered in the MC simulations.

(essentially negative charges at the top surface of AlGa_N and positive piezoelectric charges at the bottom in the AlGa_N/Ga_N heterojunction) is accounted for by means of a “virtual” background doping N_{Db} . In order to include the effect of the depletion originated by charges present in surface states, a negative charge density σ is considered at the semi-conductor-dielectric boundaries of the insulated trenches. Further details of the model can be found in Ref. 20. In this simulation, a self-consistent surface charge model is used, in which the local value of the surface charge is updated self-consistently with the carrier dynamics near the interface during the simulation, so that the surface charge at a given position is adapted to the carrier density in the nearby region.

SSDs were fabricated using an Al_{0.3}Ga_{0.7}N/GaN heterojunction (Ga-face) grown by metal oxide chemical vapor deposition (MOCVD) on a high resistivity silicon (111) substrate. The two-dimensional electron gas (2DEG) in the quantum well was 23 nm below the surface. The carrier density of the 2DEG and mobility at room temperature are $n_s = 6.04 \times 10^{12} \text{ cm}^{-2}$ and $\mu = 1200 \text{ cm}^2/\text{V s}$, respectively. The epitaxial layer consists of 5 nm of SiN (*in-situ* passivation), 23 nm of Al_{0.3}Ga_{0.7}N, 1.8 μm of GaN, and the silicon substrate thickness is 300 μm . The ohmic contacts ($R_c = 0.4 \text{ } \Omega \text{ mm}$)²¹ were formed by fast annealing Ti/Al/Ni/Au metal layers at 900 °C, then the device is isolated by ion implantation (He⁺). Due to the aspect ratio between the recess line depth (45 nm) and thickness (50 nm), specific technological steps to achieve these dimensions have been developed, mainly on the definition of the resist and the etching conditions. Using 240 nm positive poly (methyl methacrylate) (PMMA) e-beam resist thickness and inductive coupled plasma (ICP) chlorine based technology²² (average etch rate: 140 nm/min), we have realized nanodevices down to 50 nm and 90 nm for the recess and channel widths, respectively. Finally, the top metal layer (Ti/Pt/Au) is deposited to form a coplanar wave guide access line for the RF access.

As it is well known, nanodevices present high impedances. In our case, a single SSD has a typical impedance around 15 k Ω at zero bias. To overcome this limitation, many devices are fabricated in parallel without the need of any interconnection (passive structures are difficult to realize at sub-THz/THz). In this way, the extrinsic parasitic elements can be limited, which is an important feature at this frequency range. A scanning electron microscope (SEM) image of an array of 16 nanochannels is shown in Figure 2, where the overall impedance is reduced down to 1.5 k Ω .

The SEM image of a single nanochannel is shown in the inset of Figure 3. The channel width is defined by the two etched horizontal trenches and the device symmetry is broken by vertical trenches. To ensure that the current only flows through the channel, the depth of the etched trenches is enough for making them insulating. Based on surface states along the sidewalls of the trenches and electrostatic effects when biasing the device, the AlGa_N/Ga_N SSD exhibits a slightly asymmetrical current-voltage characteristic as shown in Figure 3. Once developed, the simplicity of the technological process used for the fabrication of these nanodiodes is remarkable, since it only involves the etching of insulating recess lines on a semiconductor surface. Another key aspect of these nanodevices is their planar geometry, which provides important advantages over traditional diodes (Schottky barrier) used for today’s THz systems. Figure 3 shows the good agreement between the DC measurements and MC simulations, which are able to reproduce the experimental behavior of the current, both for the high-bias (saturation) and low-bias regions. Similar agreement is obtained for nanochannels with different values of channel length and width.

To evaluate the detection responsivities of the fabricated SSDs, a Rohde & Schwarz vector network analyzer (ZVA-24) with WR 5.1 and WR 3.4 frequency extenders for G and J bands, respectively (140–220 and 220–325 GHz) has been used as signal source. No under probe setup was available beyond 325 GHz at the time of measurements so 325 GHz is the frequency limit presented here. As this kind of electronic source is composed of a multiplication chain, the measurement frequency points have been verified to be spurious free

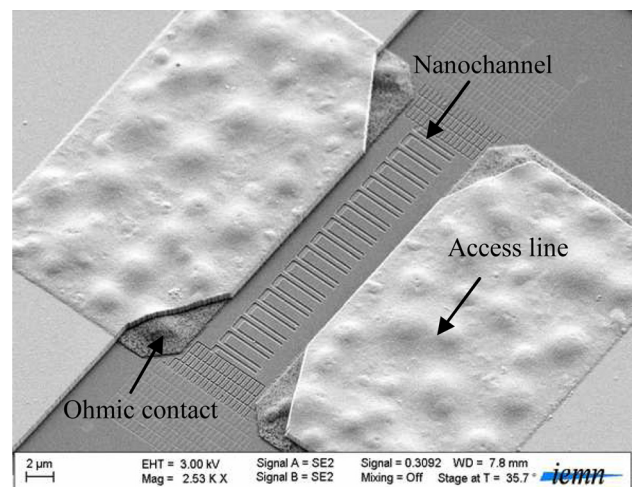


FIG. 2. SEM view of an array of 16 nanochannels.

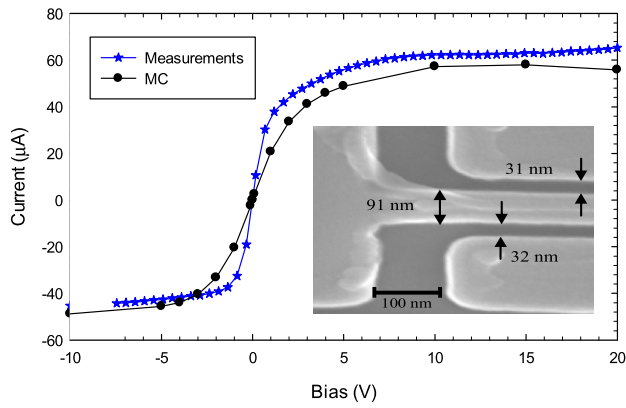


FIG. 3. Comparison of the measured I-V curve (blue stars) with the one obtained with MC simulation (black circles) corresponding to the device shown in the inset (SEM view: the length and width of the channel are about $1 \mu\text{m}$ and 90 nm , respectively).

(monochromatic signal). At each frequency point, the VNA output power was first calibrated using a PM4 calorimeter from Erickson Instruments. The signal generated by the frequency extender is applied to the nanochannels using a Cascade Microtech infinity coplanar probe within the ground-signal-ground configuration ($50 \mu\text{m}$ pitch). Probes transmission losses have been measured separately in order to determine the injected power to the nanochannel (around -25 dBm). The DC voltage across the devices is measured through the coplanar probe bias network. The frequency extender used in $140\text{--}220 \text{ GHz}$ range has less injected power compared to the $220\text{--}325 \text{ GHz}$ one, resulting in a limited signal to noise ratio at the voltmeter used for rectified signal measurement, leading to higher noise in the measured responsivities. For each measurement, the DC signal is averaged to limit the noise effects.

MC simulations of signal rectification/detection were also performed to explain the experimental results. For this sake, harmonic voltage signals of increasing frequency f are superimposed to the DC bias (V_{DC}) between the two ohmic contacts (thus, the applied voltage is $V = V_0 \sin(2\pi ft) + V_{\text{DC}}$,

with $V_0 = 0.25 \text{ V}$ and $V_{\text{DC}} = 0 \text{ V}$) and the output mean current, I_{rect} , is evaluated. We extracted first the intrinsic responsivity, S_{int} , by converting the rectified current into voltage V_{rect} (using the value of the ohmic resistance at equilibrium, R_{DC} , $V_{\text{rect}} = I_{\text{rect}} \times R_{\text{DC}}$) and dividing it by the active power dissipated at the intrinsic SSD [calculated as $P_{\text{int}} = \text{Real}(V_0^2/2Z^*)$], so that $S_{\text{int}} = V_{\text{rect}}/P_{\text{int}}$. Z is the frequency dependent complex impedance of the intrinsic SSD, which is extracted from the MC simulation taking as a base the values obtained for $I(t)$ and following.²³ Then, the extrinsic responsivity S_{ext} is obtained by means of the reflection coefficient of the device when inserted in the coplanar access line with characteristic resistance Z_0 as $S_{\text{ext}} = S_{\text{int}} \times (1 - |\Gamma|^2)$, with $\Gamma = (Z - Z_0)/(Z + Z_0)$. In our case, the measured values of Z_0 (shown in the inset of Figure 4) have been used for the calculation of the value of Γ for the lower frequencies. Above 320 GHz , a constant value of $Z_0 = (40 + 6j)\Omega$, has been considered. As we can see in Figure 4, there is a good overall agreement of extrinsic responsivity between the simulations and measurements. Also plotted are the MC results obtained by considering a constant value of $Z_0 = 50 \Omega$, showing the influence of the non ideality of the coplanar line, which reduces the responsivity at intermediate frequencies. It is also remarkable that if the value of Z_0 used in the calculations is increased to 75Ω , the value of the responsivity is significantly increased, thus showing that the responsivity of the devices can be improved by a modified design of the coplanar accesses (high impedance lines), which allow for a better power matching.

However, a strong cut off frequency is not identified in the measurements, so that 320 GHz should not be the upper operational limit of our devices. Here, the 320 GHz measurement limit was due to the available under-probe equipment. In fact, the simulations show that the devices could still be used at frequencies approaching the THz range. For example, based on the measurements, a responsivity of at least 10 V/W is still expectable beyond 600 GHz let envisage that a signal with tens of μW power level should be detectable/usable with the SSDs.

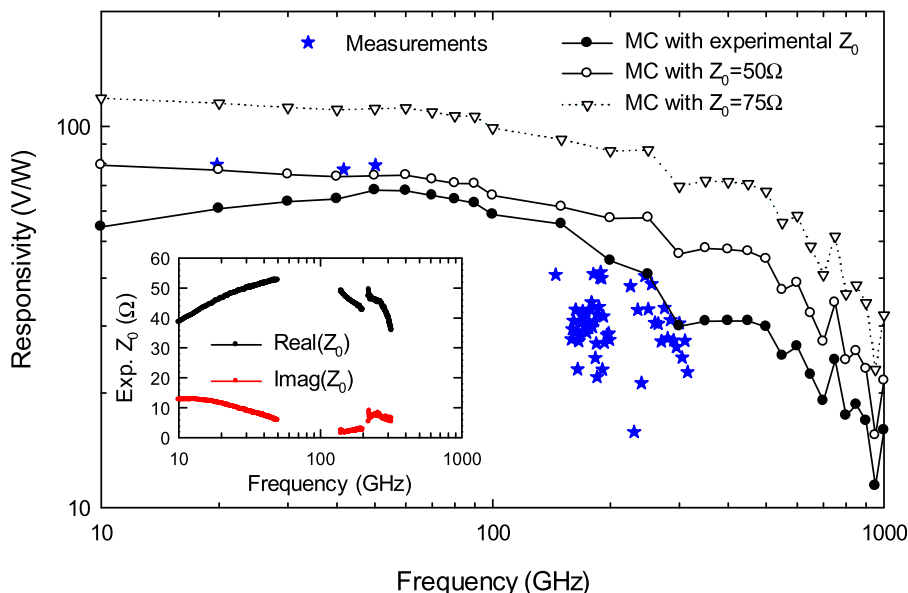


FIG. 4. Comparison of the measured (blue stars) and MC simulated extrinsic responsivity of one single GaN nanochannel. The MC results calculated using the experimental value of the characteristic impedance of the coplanar line accesses (plotted in the inset), shown in black symbols, can be compared with those obtained using real values for Z_0 corresponding to ideal lines of $Z_0 = 50 \Omega$ (white circles) and $Z_0 = 75 \Omega$ (white triangles). Measured responsivities in the $160\text{--}220 \text{ GHz}$ range are affected by noise due to a power-limitation associated to the WR 5.1 extender used as a source.

We have fabricated and tested several SSDs with different channel widths, and the best rectification (detection) is obtained for a 90 nm wide nanochannel. For wider channels, the strength of the lateral field effect induced by the two trenches is decreased, thus producing a weaker non linearity, as predicted by MC simulations.²⁴ To improve current rectification and therefore the responsivity, the channel width has to be reduced; this is not easily achieved with dry etching recess processing. To overcome this challenge and obtain effective nanochannel widths lower than $W = 90$ nm, we have replaced the etching technology by an ion implantation step²⁵ (Ar^+ ; energy: 150 keV). On the one hand, the penetration depth of the ion implantation is able to reach the GaN layer and with appropriate implant fluence and a depth profile of argon-ion implant.²⁶ The implantation energy was determined using the software Stopping and Range of Ion in Matter 2008.²⁷ In that case, the geometry of the insulating trenches is correctly defined. On the other hand, the Ar^+ implantation process induces large ion diffusion, resulting in an effective nanochannel narrower than the one defined in mask layout. However, knowing the width of the implanted regions (W_I) we can infer the effective channel width, W_{EFF} . To evaluate W_{EFF} , we have fabricated ion implanted SSDs with different projected channel widths W , from 75 to 200 nm.

By analyzing the dependence of the conductance ($1/R_{\text{DC}}$) as a function of the projected width of the channel (Figure 5(a)), we observed that the minimum width for

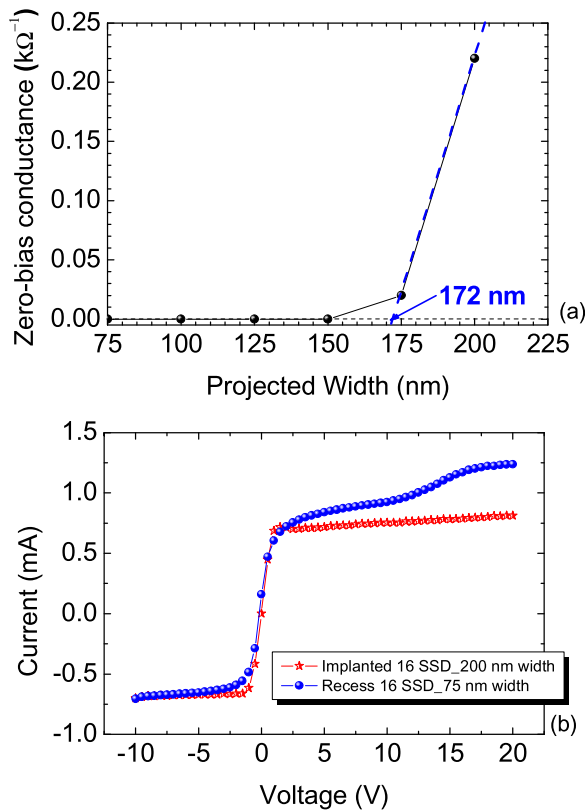


FIG. 5. (a) Dependence of the zero-bias conductance as a function of the projected width, W , of the ion implanted SSDs. (b) Comparison of the I-V curves of arrays of 16 ion implanted ($W = 200$ nm) and etched ($W = 90$ nm) SSDs for approximately the same W_{EFF} of about 30 nm.

having a conducting channel is about 172 nm. Therefore, the implantation width W_I and the possible depletion associated to the defects and surface charges created at the limits of the implanted region result in a non-conducting zone of about 86 nm at each side of the channel. To verify this assumption and compare the two technological processes, we have performed DC measurements on arrays of 16 etched and implanted SSDs with similar values of effective channel width, W_{EFF} : an implanted nanodiode with a projected width of $W = 200$ nm ($W_{\text{EFF}} \approx 28$ nm) and a recessed nanodiode with a 90 nm wide channel ($W_{\text{EFF}} \approx 30$ nm, since the depletion region in this type of devices is about 30 nm wide.¹⁸ Figure 5(b) shows that the zero bias resistance is similar and also the current saturation level. Surprisingly, the implanted devices present a much stronger saturation, which can be due to the presence of a large amount of surface states that are charged as the bias is increased, thus progressively closing the channel and counteracting the increase of the current.

Figure 6 shows the intrinsic responsivity of arrays of 16 ion implanted SSDs with different channel widths (the result for the etched SSD with $W = 90$ nm is also shown for comparison). As expected, the maximum responsivity is obtained for a projected channel width of $W = 175$ nm (corresponding to $W_{\text{EFF}} \approx 3$ nm). For channel widths lower than 175 nm, there is a very low carrier density in the channel and its resistance is very high ($\sim M\Omega$) so that the responsivity decreases sharply for the SSDs with $W = 150$ nm. Figure 6 also shows that, as expected from their analogous I-V curves [Figure 5(b)] and W_{EFF} , the responsivity of the etched SSD with $W = 90$ nm (75 nm defined on mask layout) and the implanted one with $W = 200$ nm, are very similar. SSDs, which were already demonstrated in a variety of materials, like silicon-on-insulator²⁸ and both organic²⁹ and metal oxide³⁰ thin films, are for the first time realized using this new technological process that allows us to reduce the nanochannel width. Moreover, as the insulating trenches are made of a material with high dielectric constant (the same semiconductor), the lateral field effect is improved as the effective width of the trenches is largely reduced.³¹

The array of 16 ion implanted SSDs with $W = 175$ nm is able to detect at room temperature with zero-bias a

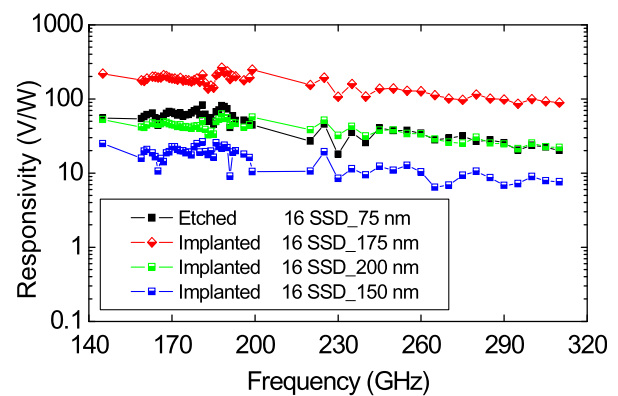


FIG. 6. Zero bias intrinsic responsivity of arrays of 16 implanted SSDs with different projected channel widths W , from 150 nm to 200 nm. Measurements for the array of etched SSDs with $W = 90$ nm are also shown for comparison.

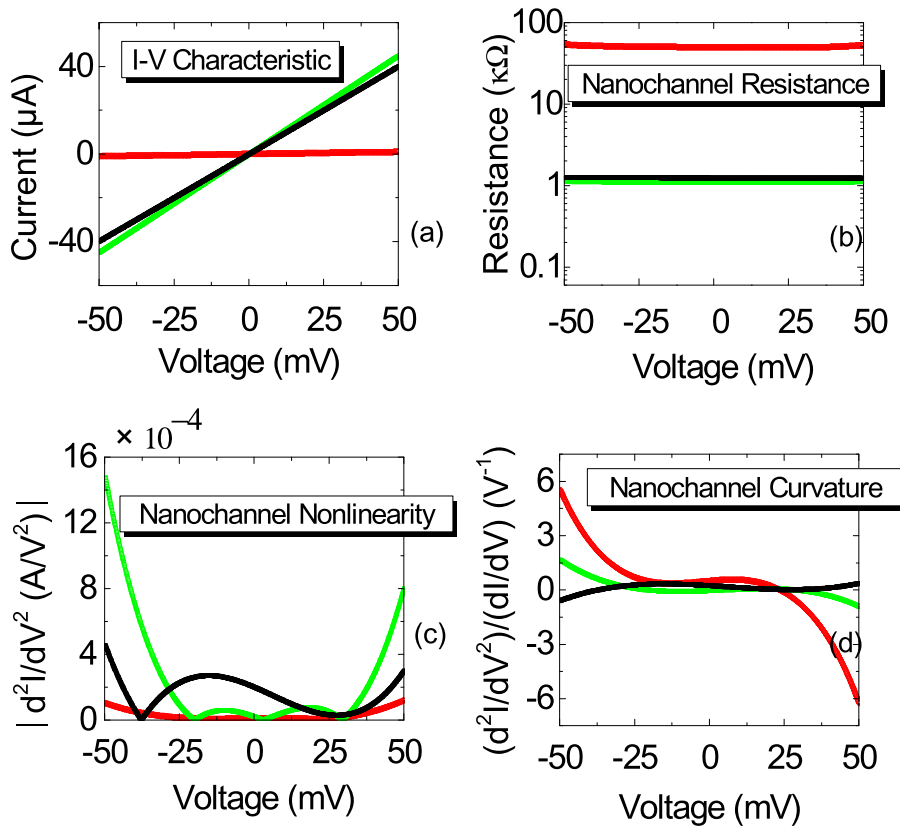


FIG. 7. Comparison of the nonlinearity of the arrays of 16 SSDs fabricated by ion implantation ($W = 200$ nm, green line, and $W = 175$ nm, red line) and etching ($W = 90$ nm, black line). (a) I-V characteristic fitted with a fifth order-order polynomial, (b) resistance, (c) nonlinearity, and (d) curvature coefficient γ .

sub-millimeter wave signal of -25 dBm power at 0.3 THz with a responsivity of 100 V/W. This value does not seem to decrease for higher frequencies, which confirms its possible operation up to THz frequencies. As our detectors operate at zero bias, the noise generated by the nanochannel is essentially due to thermal fluctuations (Johnson-Nyquist noise) since $1/f$ noise is absent at equilibrium. Therefore, the noise power spectral density per hertz is given by $4K_BTR_{DC}$, where K_B is Boltzmann's constant, T the absolute temperature, and R_{DC} the channel resistance.³² This SSD array has a resistance of approximately 50 kΩ, giving a voltage noise spectral density of ~ 28 nV/Hz^{1/2}. Using the measured responsivity, the noise equivalent power (NEP) is about 280 pW/Hz^{1/2} at 300 GHz. These results demonstrate the good performance of our ion implanted AlGaIn/GaN SSDs, with still much place for improvement using more optimized designs.

In order to explain the mechanism for the terahertz detection of the SSD, the non-linearity of their I-V characteristics has been studied. Since these are unbiased detectors, the quantities of interest are the zero bias resistance, the zero-bias non linearity, and the curvature coefficient³³ γ , which is one of the most important figures of merit for non linear applications such as high-speed switching. Taking into account the low power amplitude of THz radiation across the devices, the voltage excursion on the I-V curve has been estimated to be from -50 to $+50$ mV approximately. In this region, the I-V characteristic has been fitted with a fifth order polynomial,³⁴ Figure 7(a). Then, we have calculated the parameters corresponding to an individual SSD: resistance defined as $R = dV/dI$, plotted in Figure 7(b); non linearity

defined as the second derivative of the current³⁵ d^2I/dV^2 , Figure 7(c) and finally, the curvature coefficient defined as the ratio of the non linearity to the nanochannel conductance, $\gamma = (d^2I/dV^2)/(dI/dV)$, Figure 7(d). It appears that when decreasing the channel width of the ion implanted SSDs from $W = 200$ nm to 175 nm, the nanochannel resistance increases by several orders of magnitude leading to higher values of the curvature coefficient and therefore to a higher voltage responsivity as observed in Figure 6. The parameters for the ion implanted SSD with $W = 150$ nm are not represented as the current level was too small to fit correctly its I-V curve.

In summary, we investigated the potentialities of AlGaIn/GaN based SSDs for being used as THz detectors. We have fabricated this type of nanochannels for the first time using two different technologies, recess etch and ion implantation, and its operation as direct sub-terahertz/terahertz detectors up to 320 GHz has been demonstrated at room temperature. These nanodevices exhibit good responsivity and noise level and the results are well explained using both Monte Carlo simulations and an I-V non linearity study. Furthermore, regarding the thermal noise, which is proportional to the resistance, the noise equivalent power of our devices can be strongly reduced using larger arrays of nanochannels connected in parallel. This kind of GaN-based direct nanodetector could be a competitive candidate for nanometer scale terahertz detection.

This work has been supported by the European Commission through the ROOTHz Project No. ICT-2009-243845, by the Dirección General de Investigación (MICINN) and the

Consejería de Educación de la Junta de Castilla y León through Project Nos. TEC 2010-15413 and SA183A12-1, respectively.

- ¹*Sensing with THz Radiation*, edited by D. Mittleman (Springer-Verlag, Berlin, 2003).
- ²R. Appleby and H. B. Wallace, *IEEE Trans. Antennas Propag.* **55**, 2944 (2007).
- ³D. Grischkowsky, S. Keiding, M. van Exter, and Ch. Fattinger, *J. Opt. Soc. B* **7**, 2006 (1990).
- ⁴M. Tonouchi, *Nat. Photonics* **1**(2), 97–105 (2007).
- ⁵M. Feiginov, C. Sydlo, O. Cojocari, and Peter Meissner, *Appl. Phys. Lett.* **99**, 233506 (2011).
- ⁶S. Hargreaves and R. A. J. Lewis, *J. Mater. Sci.: Mater. Electron.* **18**(Suppl. 1), 299 (2007).
- ⁷N. Karpowicz, H. Zhong, J. Xu, K. I. Lin, J. S. Hwang, and X. C. Zhang, *Proc. SPIE* **5727**, 132 (2005).
- ⁸A. Dobroiu, M. Yamashita, Y. N. Ohshima, Y. Morita, C. Otani, and K. Rawase, *Appl. Opt.* **43**, 5637 (2004).
- ⁹A. W. M. Lee, B. S. Williams, S. Kumar, Q. Hu, and J. L. Reno, *IEEE Photonics Technol. Lett.* **18**, 1415 (2006).
- ¹⁰T. L. Hwang, S. E. Scharz, and D. B. Rutledge, *Appl. Phys. Lett.* **34**, 773 (1979).
- ¹¹E. N. Grossman and A. J. Miller, *Proc. SPIE* **5077**, 62 (2003).
- ¹²H.-W. Hübers, *IEEE J. Sel. Top. Quantum Electron.* **14**, 378 (2008).
- ¹³M. S. Vitiello, D. Coquillat, L. Viti, D. Ercolani, F. Teppe, A. Pitanti, F. Beltram, L. Sorba, W. Knap, and A. Tredicucci, *Nano Lett.* **12**, 96 (2012).
- ¹⁴M. Dyakonov and M. S. Shur, *Phys. Rev. Lett.* **71**, 2465 (1993).
- ¹⁵A. M. Song, M. Missous, P. Omling, A. R. Peaker, L. Samuelson, and W. Seifert, *Appl. Phys. Lett.* **83**, 1881 (2003).
- ¹⁶C. Balocco, A. M. Song, M. Aberg, A. Forchel, T. Gonzalez, J. Mateos, I. Maximov, M. Missous, A. Rezazadeh, J. Saijets, L. Samuelson, D. Wallin, K. Williams, L. Worschech, and H. Q. Xu, *Nano Lett.* **5**, 1423 (2005).
- ¹⁷C. Balocco, S. R. Kasjoo, X. F. Lu, L. Q. Zhang, Y. Alimi, S. Winnerl, and A. M. Song, *Appl. Phys. Lett.* **98**, 223501 (2011).
- ¹⁸A. Íñiguez-de-la-Torre, I. Íñiguez-de-la-Torre, J. Mateos, T. González, P. Sangaré, M. Faucher, B. Grimbert, V. Brandli, G. Ducournau, and C. Gaquière, *J. Appl. Phys.* **111**, 113705 (2012).
- ¹⁹J. Mateos, B. G. Vasallo, D. Pardo, and T. Gonzalez, *Appl. Phys. Lett.* **86**, 212103 (2005).
- ²⁰J. Mateos, B. G. Vasallo, D. Pardo, T. González, J. S. Galloo, Y. Roelens, S. Bollaert, and A. Cappy, *Nanotechnology* **14**, 117 (2003).
- ²¹D. Sawdai, D. Pavlidis, and D. Cui, *IEEE Trans. Electron Devices* **46**, 1302 (1999).
- ²²S. J. Pearton and D. P. Norton, *Plasma Processes Polym.* **2**, 16 (2005).
- ²³G. M. Dunn and M. J. Kearney, *Semicond. Sci. Technol.* **18**, 794 (2003).
- ²⁴I. Íñiguez-de-la-Torre, J. Mateos, D. Pardo, A. M. Song, and T. Gonzalez, *Appl. Phys. Lett.* **94**, 093512 (2009).
- ²⁵R. G. Wilson, C. B. Vartuli, C. R. Abernathy, S. J. Pearton, and J. M. Zavada, *Solid-State Electron.* **38**, 1329 (1995).
- ²⁶B. Boudart, Y. Guhel, J. C. Pesant, P. Dhamelincourt, and M. A. Poisson, *J. Raman Spectrosc.* **33**, 283 (2002).
- ²⁷J. F. Ziegler and J. P. Biersack, *The Stopping and Range of Ions in Matter* (Pergamon, New-York, 1977), Vols. 2–6.
- ²⁸G. Farhi, E. Saracco, J. Beerens, D. Morris, S. A. Charlebois, and J. P. Raskin, *Solid-State Electron.* **51**, 1245 (2007).
- ²⁹L. A. Majewski, C. Balocco, R. King, S. Whitelegg, and A. M. Song, *Mater. Sci. Eng., B* **147**, 289 (2008).
- ³⁰J. Kettle, M. Perks, and R. T. Hoyle, *Electron. Lett.* **45**, 79 (2009).
- ³¹V. Kaushal, I. Íñiguez-de-la-Torre, T. González, J. Mateos, B. Lee, V. Misra, and M. Margala, *IEEE Electron Device Lett.* **33**, 1120 (2012).
- ³²A. Van der Ziel, *Noise: Sources, Characterization, Measurement* (Prentice-Hall, Englewood Cliff, NJ, 1970).
- ³³Q. Zhou, K.-Y. Wong, W. Chen, and K. J. Chen, *IEEE Microw. Wirel. Compon. Lett.* **20**, 277 (2010).
- ³⁴M. Bareib, B. N. Tiwari, A. Hochmeister, G. Jegert, U. Zschieschang, H. Klauk, B. Fabel, G. Scarpa, G. Koblmuller, G. H. Bernstein, W. Porod, and P. Lugli, *IEEE Trans. Microwave Theory Tech.* **59**, 2751 (2011).
- ³⁵A. M. Cowley and H. O. Sorensen, *IEEE Trans. Microwave Theory Tech.* **14**, 588 (1966).